

Effect of Sn Addition, Process Atmosphere pO_2 , and Annealing Time on the Selective Oxidation of a C-2Mn-1.7Si (Wt Pct) Advanced High-Strength Steel During Continuous Galvanizing



G. SEYED MOUSAVI, B. LANGELIER, and J.R. MCDERMID

The effects of process atmosphere pO_2 , annealing time, and a minor Sn addition on the selective oxidation of a Fe-0.1C-2Mn-1.7Si (wt pct) advanced high-strength steel during continuous galvanizing heat treatments were determined. The reference and 0.05 wt pct Sn-added steels were intercritically annealed at 1113 K (840 °C) for annealing times between 60 and 600 seconds in a N₂-5 vol pct H₂ gas atmosphere, where the process atmosphere pO_2 was controlled by varying the dew points at 223 K, 243 K, and 278 K (−50 °C, −30 °C and +5 °C). It was found that both the internal and external oxidation kinetics followed a parabolic rate law and were significantly reduced by the Sn addition to the alloy. For the lowest pO_2 223 K (−50 °C) dew point atmosphere, the external oxides comprised compact, film-like MnSiO₃, SiO₂, and granular MnO. The addition of Sn to the alloy reduced the compactness of the granular oxides. Increasing the atmosphere dew point to 243 K and 278 K (−30 °C and +5 °C) reduced the thickness of the external oxides and increased the depth of internal oxidation for both alloys. Under the highest pO_2 278 K (+5 °C) dew point atmosphere, although the reference steel surface was covered with small, closely packed MnSiO₃ nodule-like particles, the addition of Sn altered their morphology to larger, more widely spaced nodules and decreased the depth of internal oxidation. The effect of Sn was found to be the result of its segregation at the surface oxide/substrate interface, as shown by 3D atom probe tomography. The alterations in oxide morphology resulting from the Sn addition are expected to enhance the reactive wetting of the substrate surfaces by the continuous galvanizing bath.

<https://doi.org/10.1007/s11661-019-05202-3>

© The Minerals, Metals & Materials Society and ASM International 2019

I. INTRODUCTION

ONE of the most intense fields of study by the steel industry since the mid-1990s has been the galvanizing of advanced high-strength steels (AHSS), which can be challenging due to the selective oxidation of the alloying elements required to achieve the desired microstructures and properties during annealing prior to galvanizing in the commonly employed continuous galvanizing line (CGL) process atmosphere of N₂-(5 to 20 vol pct) H₂- x H₂O.^[1–5] The morphology, spatial distribution, and chemistry of these oxides on the substrate surface indicate whether the desired η -Fe₂Al₅Zn_x interfacial layer can form and whether the finished coating is

acceptable.^[1–4] For example, it has been established by several authors^[4–12] that the presence of film-like external oxides can block the reaction between the substrate Fe and the bath dissolved Al to form the required η -Fe₂Al₅Zn_x interfacial layer, characteristic of reactive wetting having occurred. However, the presence of either thin film-like or widely distributed nodule-like external oxides can promote contact between the substrate Fe and bath Al to facilitate the formation of the η -Fe₂Al₅Zn_x interfacial layer through mechanisms such as aluminothermic reduction, oxide lift-off, and bath infiltration between the oxide and substrate, thereby leading to high-quality Zn coatings during continuous galvanizing.

Several authors have proposed processing methods to alter the external oxide chemistry and morphology to facilitate reactive wetting of AHSS surfaces by the continuous galvanizing bath. For example, annealing under higher process atmosphere oxygen partial pressures (pO_2) (*i.e.*, higher dew points)^[13–16] and applying the oxidation-reduction process^[17,18] have been reported to favorably modify surface oxide characteristics and,

G. SEYED MOUSAVI and J.R. MCDERMID are with the Steel Research Centre, McMaster University, Hamilton, ON L8S 4L8, Canada. Contact e-mail: mcdermid@mcmaster.ca B. LANGELIER is with the Department of Materials Science and Engineering, McMaster University, Hamilton, ON L8S 4L8, Canada.

Manuscript submitted October 18, 2018.

Article published online March 29, 2019

consequently, improve the reactive wetting of AHSSs. Another recently advocated approach to modifying the external oxide morphology is the addition of surface-active elements such as Bi, Sn, and Sb to the steel composition. These elements have a strong tendency to segregate to the steel surface and grain boundaries in order to decrease the local elastic lattice strain energy, attributed to their larger atomic radius compared to the substrate.^[19,20] This segregation can also decrease the substrate surface energy, as shown by Seah and Hondros^[21] in the case of adding Sn to pure iron.

Several studies have examined the effect of Sn^[22–25] and Sb^[26–30] on the surface and subsurface oxide characteristics arising from annealing. Lyudkovsky^[26] added up to 0.08 wt pct Sb to a 0.02C-4Mn-1Si-2Al (wt pct) steel and showed that the most significant drop in the depth of internal oxidation could be achieved when the concentration of Sb was between 0.015 and 0.055 wt pct. Below and above this range, Sb had very little effect on oxidation. Cho *et al.*^[24] showed that, in the case of the addition of Sn to a 0.1C-1.6Mn-1.5Si (wt pct) TRIP steel, the external oxide morphology was altered from film-like to lens-shaped particles, thereby improving the reactive wetting of the substrate by a Zn-0.22Al (wt pct) continuous galvanizing bath considerably. Cho *et al.*^[25] also reported that changes in the oxide morphology could be attributed to changes in the oxide-substrate interfacial energy arising from the addition of Sn to the steel chemistry. In addition, the authors observed a reduction in the external oxide Si/Mn ratio, which was attributed to the occupation of potential oxygen adsorption sites and a consequent reduction in the oxygen permeability of the surface. It is noteworthy that although Cho *et al.*^[25] have performed the aforementioned study by adding Sn to their base TRIP composition in the range of 0.05 to 1 wt pct, in order to maintain the mechanical properties of the steel, it is generally accepted that the Sn addition to steels be a maximum of 0.1 wt pct in order to avoid hot shortness.^[31,32]

More recently, Pourmajidian *et al.*^[33] considered the combined effect of a 0.05 wt pct Sn addition and annealing parameters—*i.e.*, annealing time and annealing atmosphere pO_2 —on the selective oxidation of a 0.1C-6Mn-2Si (wt pct) medium-Mn third-generation AHSS. They reported a reduction in the kinetics of both external and internal oxidation after the addition of Sn to the steel chemistry as a result of Sn segregation to the steel surface and its consequent effect on reducing the oxygen flux into the substrate. The interfacial Sn enrichment was determined to be a 10-fold increase compared to its bulk value, using 3D atom probe tomography.

It should be pointed out that, except for the research of Pourmajidian *et al.*,^[33] the vast majority of studies to date on the effect of Sn on the selective oxidation and reactive wetting of AHSSs are restricted to a specific set of experimental annealing parameters with a fixed process atmosphere pO_2 . Thus, the objective of the present study is to determine the effects of annealing atmosphere pO_2 , annealing time, and the addition of 0.05 wt pct Sn on the external and internal selective

oxidation of an intercritically annealed Fe-0.1C-2 Mn-1.7Si (wt pct) AHSS within the context of application to the continuous galvanizing process.

II. EXPERIMENTAL PROCEDURE

Two series of CMnSi steels, referred to as Reference and Sn-added in the subsequent text, were fabricated with the chemical composition shown in Table I for use in the present study.

1.2-mm-thick cold-rolled steel sheets were cut into 10 mm × 50 mm coupons with their longitudinal axis parallel to the sheets' rolling direction. All coupons were ground with 1200 grit SiC paper to mitigate the effect of surface roughness on subsequent surface analysis. Experimental heat treatments were executed in the McMaster Galvanizing Simulator (MGS, Iwatani Surtec) at an intercritical temperature of 1113 K (840 °C), in a N₂-5 vol pct H₂ process atmosphere and under three different dew points (dp) of 223 K, 243 K, and 278 K (−50 °C, −30 °C and +5 °C). A detailed summary of the experimental process atmospheres, including their pO_2 at the intercritical annealing temperature, is presented in Table II.

Experimental samples were initially heated to 773 K (500 °C) at a heating rate of 15 K/s and to the intercritical annealing temperature (IAT) of 1113 K (840 °C) at a heating rate of 5 K/s. In order to investigate the effect of annealing time on selective oxidation, samples were held at the IAT for 60, 120, 240, 360, and 600 seconds. Samples were then cooled to 738 K (465 °C) at 20 K/s, held for 20 seconds to promote thermal equilibrium within the thickness of the sample, and were eventually cooled at 20 K/s to room temperature by N₂ jet cooling. In all cases, the sample thermal profile was controlled by a 0.5-mm type K thermocouple welded to a coupon. All heat treatments employed triplicate samples. Immediately upon removal from the MGS, samples were stored in anhydrous isopropanol in order to mitigate further oxidation.

Several analytical techniques across a variety of length scales were used to investigate various aspects of the experimental steels' selective oxidation and to cross-correlate the results.

In order to determine the thickness of oxides as well as the mode of oxidation of Mn and Si as a function of annealing parameters and the Sn addition, on a mesoscopic scale, elemental depth profiling was carried out using X-ray photoelectron spectroscopy (XPS) (PHI Quantera, Physical Electronics, Chanhassen, MN) with an Al K α X-ray source (1486.6 eV). A 100 μm × 100 μm area was analyzed on each sample. The elemental depth profiles are considered accurate to ± 5 pct of the measured value in atomic percent. Oxide speciation was determined *via* binding energy analysis and comparison to the appropriate standards. It should be noted that depth profiles were started after sputtering such that no significant C peak, arising from sample contamination during exposure to the ambient atmosphere, was present. All XPS data were processed using the

Table I. Chemical Composition of Experimental Steels (Wt Pct)

| Steel | C | Mn | Si | Al | Ti | N | S | Sn | Fe |
|-----------|------|------|------|------|------|-------|-------|-------|---------|
| Reference | 0.10 | 2.03 | 1.76 | 0.04 | 0.01 | 0.004 | 0.002 | 0.005 | balance |
| Sn-Added | 0.11 | 2.04 | 1.75 | 0.04 | 0.01 | 0.003 | 0.002 | 0.05 | balance |

Table II. Experimental Process Atmospheres

| Process Atmosphere dp [K (°C)] | N ₂ Content (Vol Pct) | H ₂ Content (Vol Pct) | pH ₂ O/pH ₂ | pO ₂ at 1113 K (840 °C) (atm) |
|--------------------------------|----------------------------------|----------------------------------|-----------------------------------|--|
| 223 (−50) | | 95 | 5 | 0.0010 |
| 243 (−30) | | 95 | 5 | 0.0082 |
| 278 (+5) | | 95 | 5 | 0.1380 |

MultiPak software (Version 6). The metallic Fe2p_{2/3} binding energy was used to calibrate all spectra.

The morphology, size, and spatial distribution of the external oxides during the annealing heat treatments were analyzed using a JEOL 7000F field emission gun scanning electron microscope (FEG-SEM). Prior to imaging, all samples were coated with 5-nm-thick layer of Pt to avoid charging.

In order to measure the thickness of the external oxides and the depth of internal oxidation as a function of annealing time—*i.e.*, determine the external and internal oxidation kinetics—focussed ion beam (FIB, NVision 40 by Zeiss) milling and image analysis were employed. In this case, at least two 15- μ m-wide trenches were cut randomly on the cross section of each oxidized sample. Using a grid system, approximately 100 measurements of the external oxide thickness and internal oxidation depth were carried out on each sample using ImageJ 1.42q software. The data were then averaged for the purposes of the kinetic study. It should be noted that the error bars presented in the kinetic study represent the 95 pct confidence interval of the mean in all cases. A more detailed explanation of this methodology is available elsewhere.^[33]

In order to analyze the fine-scale structure of the external and internal oxides, a transmission electron microscope (TEM) integrated with a Gatan 865 electron energy loss spectroscopy (EELS) spectrometer was applied. TEM samples were fabricated *via* FIB lift-outs and standard preparation techniques across the external oxide-substrate interface, where the oxide was protected during FIB milling *via* C and W deposits. The resultant samples were then analyzed using a FEI Titan 80 300 TEM using an acceleration voltage of 300 keV, where the energy resolution in monochromated mode was tuned to 0.08 eV full width half-maximum (FWHM) at the zero-loss peak. The obtained EELS spectra were processed using Gatan Digital Micrograph 2.3.

3D atom probe tomography (3D APT) across the external oxide-substrate interface was carried out using a Cameca LEAP 4000X HR atom probe. APT samples were prepared by sputter coating the sample surface with a 400-nm-thick Cr or Ni layer followed by APT needle preparation using established FIB lift-out

procedures^[34] and a 30 keV Ga ion beam, with final cleaning performed at 10 keV. The sharpened tips were analyzed using laser pulse mode ($\lambda = 355$ nm) with pulse energy of 60 or 90 pJ/pulse at a base temperature of approximately 60 K or 76 K for the as-received Sn-added and annealed Sn-added samples, respectively. The target detection rate was set at 0.003 ions/pulse (0.3 pct) which was maintained by an applied DC voltage. The laser pulsing rate was 125 and 200 kHz for the as-received Sn-added and annealed Sn-added samples, respectively. The data obtained were subsequently processed using IVAS v3.8 software.

III. RESULTS

XPS elemental depth profiles of the Reference and Sn-added steels annealed under the three process atmospheres (Table II) are shown in Figure 1. It should be noted that, for the sake of simplicity, the XPS results presented here were confined to annealing times of 60, 120, and 600 seconds.

In the case of the Reference steel, for the lowest pO₂ process atmosphere [*i.e.*, 223 K (−50 °C) dp, Table II] and annealing time of 60 seconds, enrichment of both Si and Mn was observed on the surface and in the subsurface (Figure 1(a)) to a depth of approximately 350 nm, where their concentrations reduced to their bulk concentrations (*i.e.*, 3.4 and 2.0 at. pct, respectively). This is while for the Sn-added steel annealed for 60 seconds at the same pO₂, Si showed only surface enrichment, indicative of the occurrence of external oxidation only (Figure 1(a)). Comparable observations can be made for the samples annealed for 120 seconds (Figure 1(b)). Holding the experimental steel at the intercritical annealing temperature for 600 seconds led to an increase in the external oxide thickness as well as the depth internal oxidation (Figure 1(c)) for both steels. However, the Sn-added steel continued to show minimal internal oxidation for the 600-second annealing time (Figure 1(c)).

Increasing the process atmosphere pO₂ using the 243 K (−30 °C) dp (Table II), in the case of the Reference steel, resulted in a decrease in the thickness of the

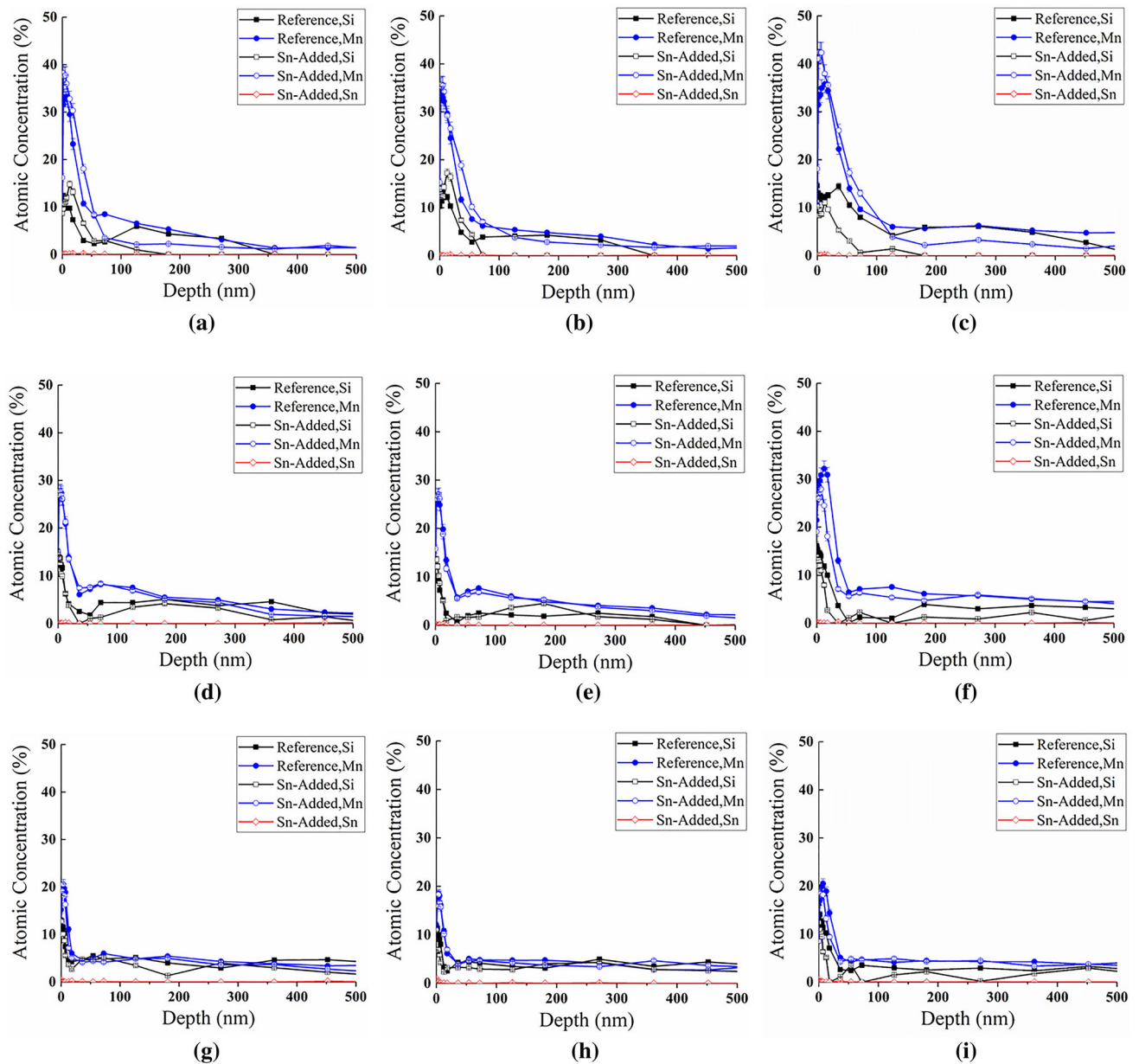


Fig. 1—XPS elemental depth profiles of the Reference and Sn-added steels as a function of annealing time and process atmosphere pO_2 : (a) 223 K ($-50\text{ }^\circ\text{C}$) dp for 60 s, (b) 223 K ($-50\text{ }^\circ\text{C}$) dp for 120 s, (c) 223 K ($-50\text{ }^\circ\text{C}$) dp for 600 s, (d) 243 K ($-30\text{ }^\circ\text{C}$) dp for 60 s, (e) 243 K ($-30\text{ }^\circ\text{C}$) dp for 120 s, (f) 243 K ($-30\text{ }^\circ\text{C}$) dp for 600 s, (g) 278 K ($+5\text{ }^\circ\text{C}$) dp for 60 s, (h) 278 K ($+5\text{ }^\circ\text{C}$) dp for 120 s, and (i) 278 K ($+5\text{ }^\circ\text{C}$) dp for 600 s.

external oxides and an increase in the depth of the internal oxidation (Figures 1(d) and (e)) for the 60- and 120-second annealing times compared to the same steel annealed under the 223 K ($-50\text{ }^\circ\text{C}$) dp process atmosphere (Figures 1(a) and (b)). Although the addition of Sn to the steel did not significantly affect the thickness of the external oxides after the 60 and 120 seconds anneal (Figures 1(d) and (e)), it did appear to have resulted in a slight decrease in the thickness of the external oxides after annealing for 600 seconds (Figure 1(f)).

For the highest pO_2 process atmosphere (278 K ($+5\text{ }^\circ\text{C}$) dp, Table II), after annealing for 60 and 120 seconds, a further reduction in the thickness of the

external oxides and increase in the depth of internal oxidation were observed for both the Reference and Sn-added steels (Figures 1(g) and (h)) compared to the lower pO_2 process atmospheres for the same annealing times. It can also be seen that, for both experimental steels, the thickness of the external oxides increased slightly with increasing annealing time to 600 seconds arising from diffusion-based growth of the oxides (Figure 1(i)). In addition, for all annealing times, no significant change was observed in the thickness of the external oxides between the Sn-added and the Reference steel (Figures 1(g) through (i)). It should be noted that no significant Sn segregation could be observed in the

XPS elemental profiles of the Sn-added steels for all annealing times and process atmosphere pO_2 due the inability of XPS to detect Sn at these low concentrations.^[35]

Figures 2(a) and (b) show the growth kinetics of the external and internal oxides, respectively, as a function of process atmosphere pO_2 and Sn addition, as determined using the FIB trench cut methodology described above. As can be seen, for both the Reference and Sn-added steels under all of the process atmosphere pO_2 explored, the external oxide thickness and internal oxidation depth kinetics obeyed a parabolic rate law, indicative of solid-state diffusion-controlled oxidation.^[36] It is noteworthy that the coefficient of determination (*i.e.*, R^2 value) of the regression lines was greater than 0.79 for all of the data presented in Figure 2. Moreover, increasing the annealing atmosphere pO_2 via increasing the process atmosphere dew point resulted in a decrease in the thickness of the external oxides (Figure 2(a)) and an increase in the depth of internal oxidation (Figure 2(b)), characteristic of the transition from internal to external oxidation per the classic Wagner model.^[37] In addition, it can be seen that, for all process atmosphere pO_2 , the rates of both external and internal oxidation were decreased significantly by the addition of Sn to the substrate for a given process

atmosphere pO_2 . This result is further highlighted in Figure 3, which shows the variation in the parabolic rate constant (k_p) with process atmosphere and substrate composition for external (Figure 3(a)) and internal oxidation (Figure 3(b)), respectively.

From Figure 3(a), it can be seen that the rate constants for external oxidation decreased significantly for both the Reference and Sn-added substrates with increasing the process atmosphere pO_2 from 223 K (-50°C) dp to the 243 K (-30°C) dp, after which the value of k_p did not change significantly for the highest pO_2 278 K ($+5^\circ\text{C}$) dp process atmosphere. These trends are consistent with the transition from external to internal oxidation with increasing process atmosphere pO_2 , as characterized by the significantly increased rate of internal oxidation seen in Figure 2(b) and the significantly increased values of the rate constant for internal oxidation shown in Figure 3(b), coupled with the consummate decrease in the rate of external oxidation and decline in k_p for external oxidation with increasing process atmosphere pO_2 , per Figures 2(a) and 3(a). Thus, the significantly different and larger k_p values for external oxidation for the 223 K (-50°C) dp process atmosphere and their decline to very small and insignificantly different values for the higher pO_2 process atmospheres (Figure 3(a)) can be attributed to the switch in the dominance of external to internal oxidation for the higher pO_2 process atmospheres, consistent with the increase in k_p observed for internal oxidation and the very low value for the k_p for internal oxidation observed for the lowest pO_2 process atmosphere (Figure 2(b)).

However, for both steels and the majority of the process atmosphere pO_2 explored, the external and internal oxidation kinetics and k_p values for the Sn-added steel were significantly lower than those observed for the Reference alloy, indicating that the 0.05 wt pct Sn addition significantly lowered the transport of O into the steel and/or Mn/Si to the oxidation front, as previously suggested by Cho *et al.*^[25] Similar results were reported by Pourmajidian *et al.*^[33] with respect to the effect of the addition of 0.05 wt pct Sn to a 0.1C-6Mn-2Si (wt pct) medium-Mn AHSS on external and internal (Mn,Si)-oxide growth kinetics.

Figures 4, 5, and 6 show the morphology and distribution of the external oxides formed on the surface of the Reference and Sn-added steels after being intercritically annealed under the 223 K (-50°C) dp, 243 K (-30°C) dp, and 278 K ($+5^\circ\text{C}$) dp process atmospheres, respectively, for annealing times of 120 and 600 s.

Per Figure 4, annealing the Reference steel under the lowest pO_2 process atmosphere (*i.e.*, 223 K (-50°C) dp, Table II) for 120 seconds resulted in the formation of closely packed patches of compact granular oxides with areas in between these oxide patches consisting of thinner, film-like oxides (Figure 4(a)). However, in the case of the Sn-added steel, although the same general oxide morphology was observed, the patches of granular oxides were relatively widely spaced and the steel surface comprised larger area fractions of the film-like oxides compared to the Reference steel (Figure 4(b)).

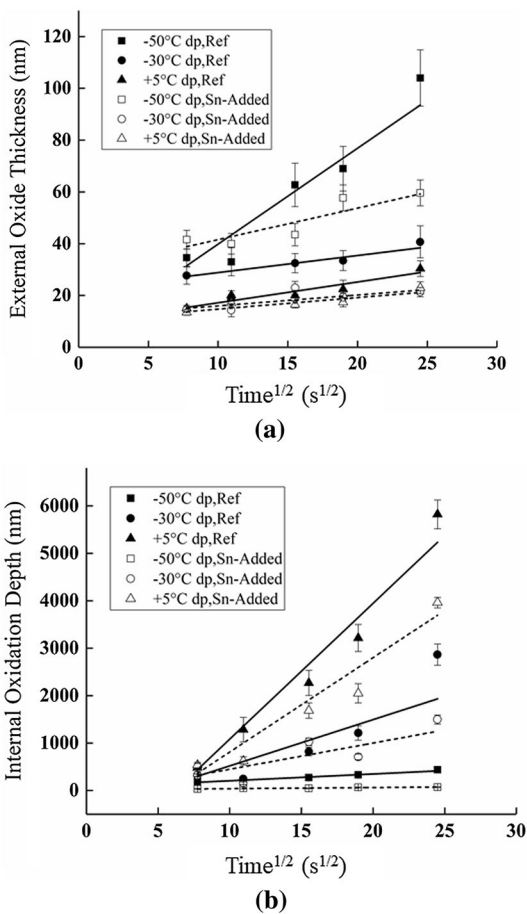


Fig. 2—Growth kinetics of (a) external oxides and (b) internal oxides formed during annealing the Reference and Sn-added steels as a function of process atmosphere.

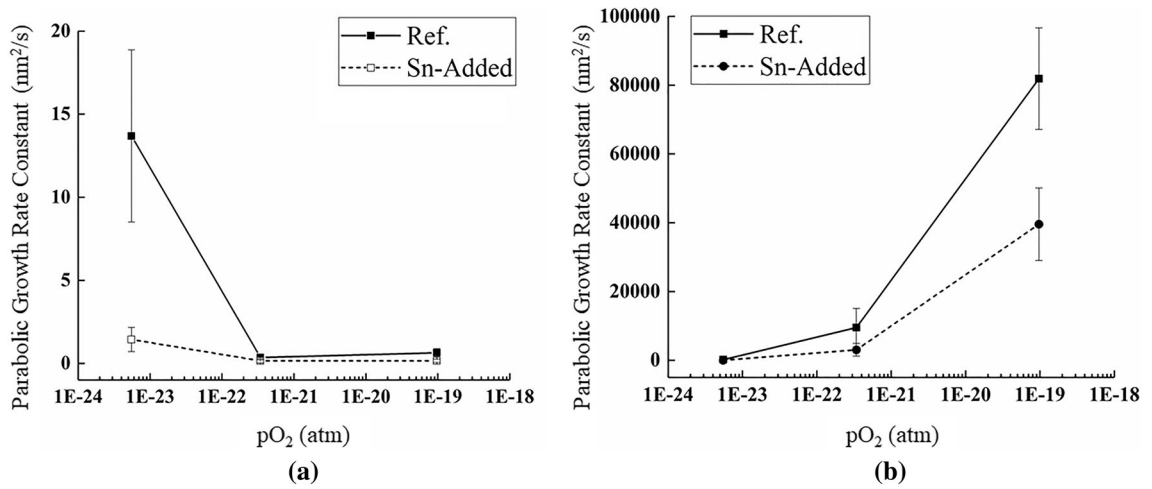


Fig. 3—Parabolic growth rate constants for the Reference and Sn-added steel selective oxidation: (a) external oxidation; (b) internal oxidation.

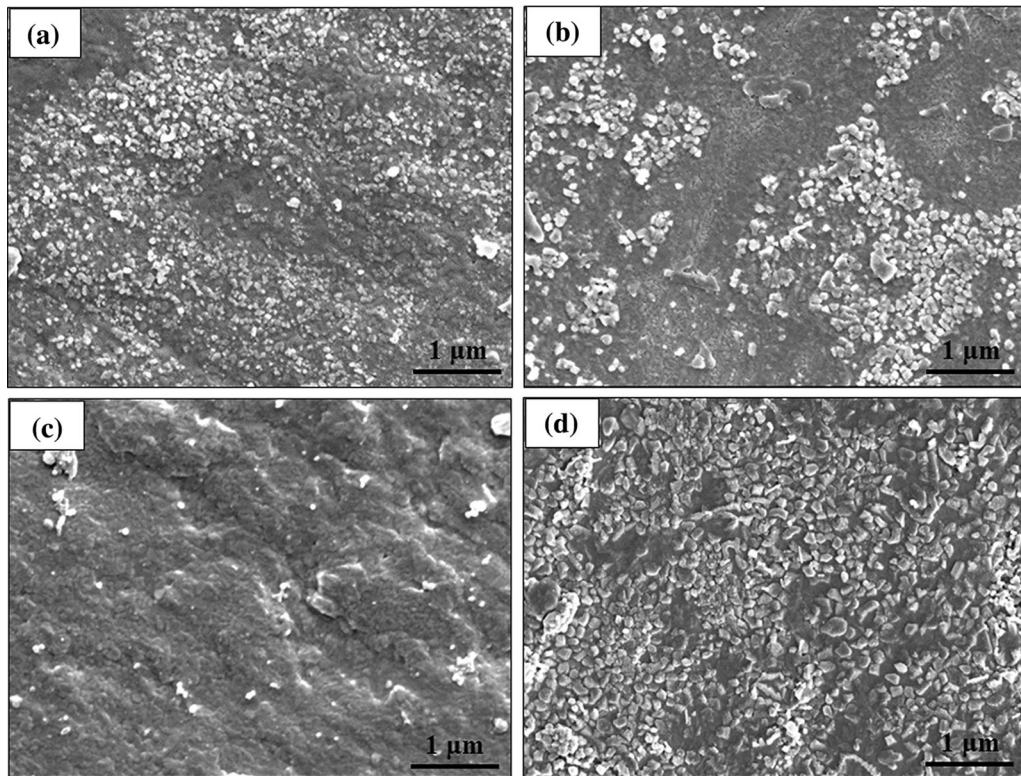


Fig. 4—SEM images of the Reference and Sn-added steel surfaces annealed under the 223 K (−50 °C) dp process atmosphere as a function of annealing time: (a) Reference steel, 120 s, (b) Sn-added steel, 120 s, (c) Reference steel, 600 s, and (d) Sn-added steel, 600 s.

Annealing the steel for 600 seconds led to the formation of compact, film-like oxide on the Reference steel (Figure 4(c)) and an increase in surface coverage and coarsening of the oxides on the Sn-added steel (Figure 4(d)), as would be expected due to the diffusion-based growth of the oxides during prolonged annealing. These results are generally consistent with the trends seen in the XPS results in Figures 1(a) through (c) and the external oxidation kinetic data presented in Figure 2.

As can be seen in Figure 5, increasing the process atmosphere pO₂ to the 243 K (−30 °C) dp (Table II) led to the formation of compact, film-like external oxides on the surface of the Reference steel after 120 seconds of intercritical annealing (Figure 5(a)). Increasing the annealing time to 600 seconds resulted in an increase in the compactness of the external oxides (Figures 5(c) and (d)). However, although these external oxides exhibited a film-like morphology on the Reference steel (Figures 5(a) and (c)), the addition of Sn to the steel

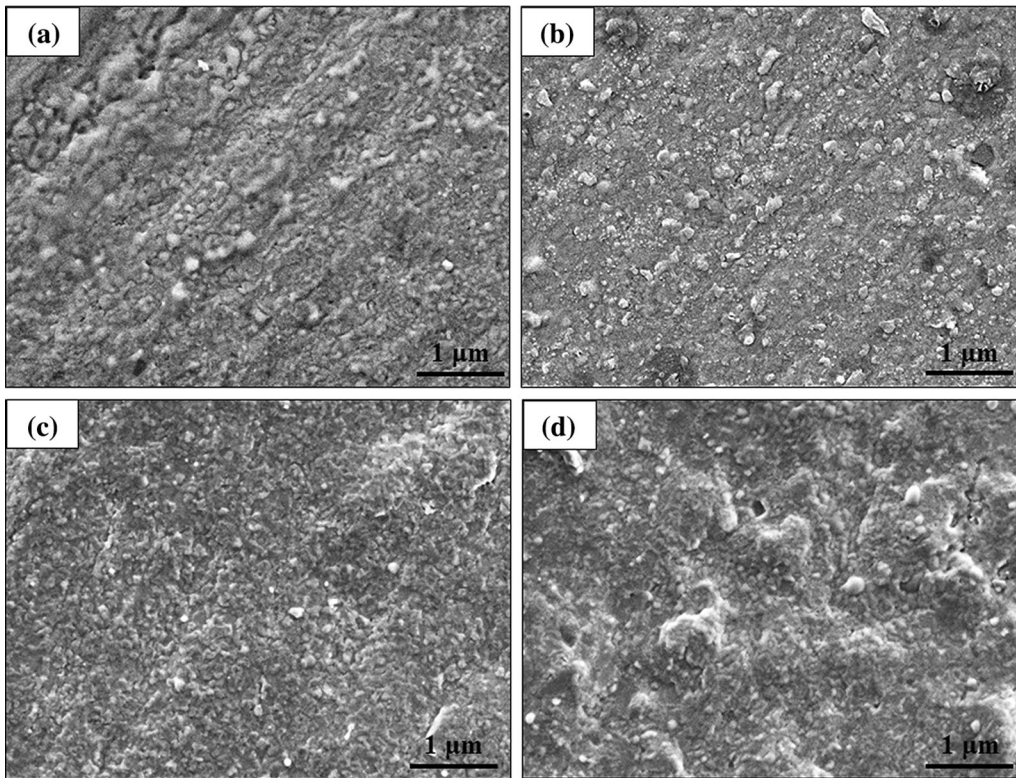


Fig. 5—SEM images of the Reference and Sn-added steel surfaces annealed under the 243 K ($-30\text{ }^{\circ}\text{C}$) dp process atmosphere as a function of annealing time: (a) Reference steel, 120 s, (b) Sn-added steel, 120 s, (c) Reference steel, 600 s, and (d) Sn-added steel, 600 s.

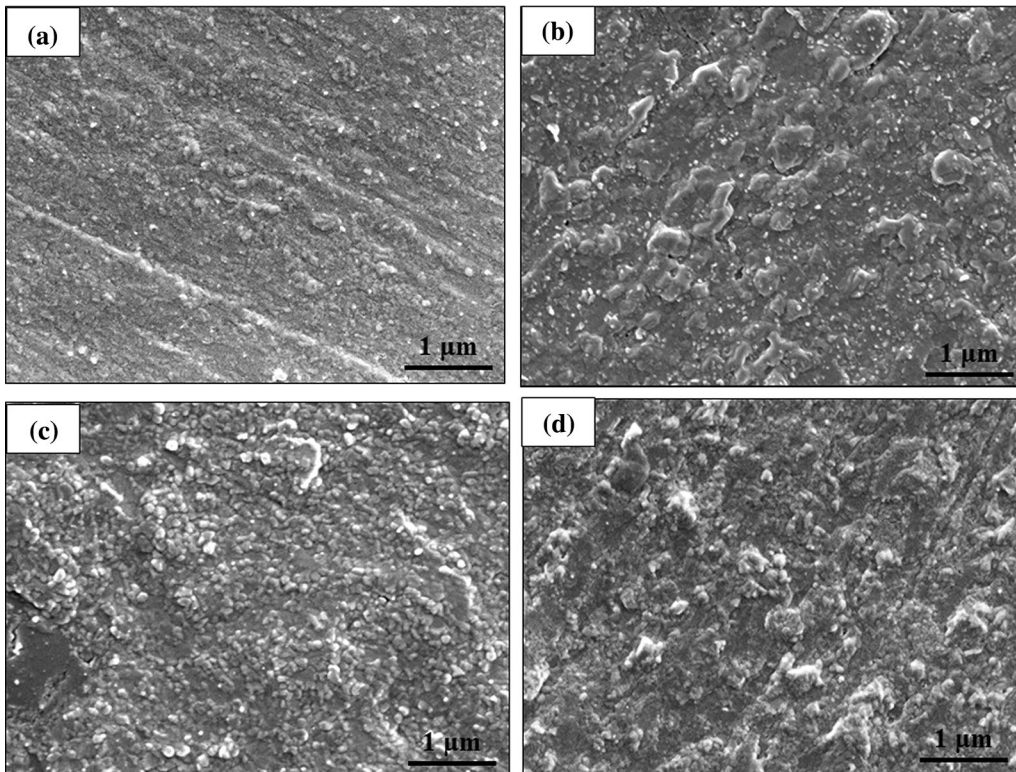


Fig. 6—SEM images of the Reference and Sn-added steel surfaces annealed under the 278 K ($+5\text{ }^{\circ}\text{C}$) dp process atmosphere as a function of annealing time: (a) Reference steel, 120 s, (b) Sn-added steel, 120 s, (c) Reference steel, 600 s, and (d) Sn-added steel, 600 s.

altered their morphology to nodular particles (Figures 5(b) and (d)).

From Figure 6, it can be seen that annealing the Reference steel under the highest pO_2 process atmosphere of 278 K (+5 °C) dp (Table II) for 120 seconds significantly modified the external oxide morphology from the relatively compact, granular oxides with small fractions of interspersed films observed for the lowest pO_2 process atmosphere of 223 K (−50 °C) dp (Figure 4(a)) and compact, film-like oxides observed for the intermediate pO_2 process atmosphere of 243 K (−30 °C) dp (Figure 5(a)) to a combination of film-like and fine, closely spaced nodule-like particles (Figure 6(a)). Adding Sn to the steel, however, significantly changed the morphology of the oxides to large, widely spaced nodule-like particles (Figure 4(b)). As reported by Bellhouse and McDermid,^[6] the existence of large, widely spaced oxide nodules on the surface of the steel can have benefits in promoting good reactive wetting, which the authors attributed to the formation of Fe-Al intermetallics between the oxide nodules. Significant coarsening of the external oxides for the Sn-added alloy was observed for the longer annealing time of 600 seconds (Figure 6(d)), as would be expected given the diffusional nature of external oxide growth.

TEM was used to characterize the fine-scale microstructure of the external and internal oxides. Due to the importance of the 120-second annealing time to the industrial continuous galvanizing process, the TEM results presented herein have been confined to this

annealing time as a function of process atmosphere pO_2 . Figures 7(a) and (b) show TEM cross-sectional micrograph of the Reference and Sn-added steels annealed under the lowest pO_2 223 K (−50 °C) dp process atmosphere (Table II), respectively, along with the Mn-L_{2,3}, O-K and Si-K edge EELS spectra (Figure 7(c)) of the points labeled as 1, 2, and 3 in Figure 7(a). It should be noted that the dark area above the oxides in Figures 7(a) and (b) correspond to the C film deposited on the sample prior to FIB milling. Per Figure 7(a), a two-layer 33 ± 5-nm-thick external oxide can be seen on the surface of the Reference steel. A comparison between the features of the Mn-L_{2,3}, O-K, and Si-K edges with the standard MnSiO₃, Mn₂SiO₄,^[38] MnO,^[39] and SiO₂^[40] EELS spectra revealed that the compact granular external oxides corresponded to MnO and the oxides at the steel/oxide interface corresponded to MnSiO₃. The darkest oxide, demarcated as point 3 in Figure 7(a), was determined to be SiO₂. On the other hand, per Figure 7(b), a 40 ± 4-nm-thick multi-layer external oxide formed on the Sn-added steel, with granular particles located farther apart compared to the Reference steel (Figure 7(a)). The top, middle, and bottom oxides corresponded to MnO, MnSiO₃, and SiO₂, respectively. The formation of less compact granular oxides on the surface of the Sn-added steel compared to the Reference steel is consistent with the SEM observations in Figures 4(a) and (b). Comparing Figures 7(a) and (b), it can be seen that the internal oxides formed in the Reference steel (Figure 7(a)) were

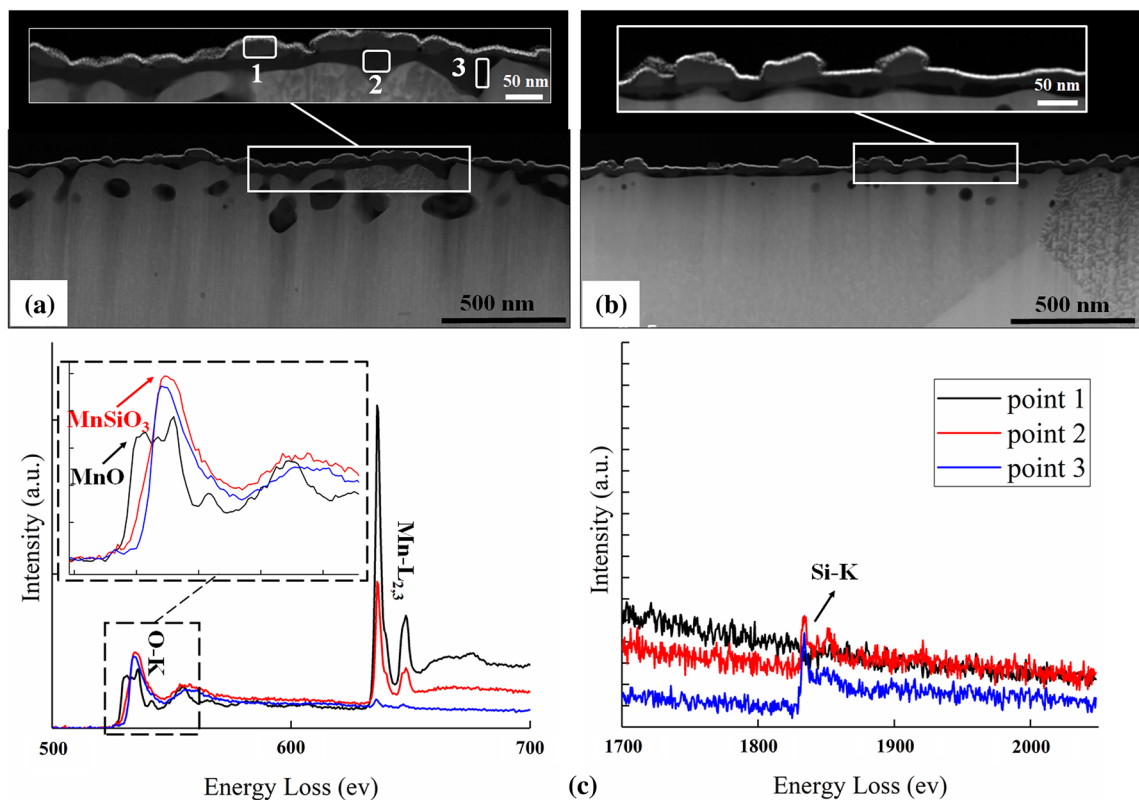


Fig. 7—TEM cross-sectional micrograph of the (a) Reference steel and (b) Sn-added steel annealed under the 223 K (−50 °C) dp process atmosphere. (c) Mn-L_{2,3}, O-K, and Si-K edge electron energy loss spectra of points 1 through 3 in (b).

larger and were located deeper into the subsurface compared to those of the Sn-added steel (Figure 7(b)), as was observed in the XPS elemental profiles (Figure 1(a)). The internal oxides were identified as MnSiO_3 closer to the surface and a mixture of MnSiO_3 and SiO_2 deeper in the subsurface in both steels.

Figure 8 shows TEM views across the external oxide interface and subsurface of the Reference and Sn-added steels after annealing under the 243 K and 278 K (-30°C and $+5^\circ\text{C}$) dp process atmospheres for 120 seconds. As previously observed with the XPS data (Figure 1) and internal oxidation kinetics study (Figure 2(b), 3 and Table II), increasing the annealing atmosphere $p\text{O}_2$ resulted in a significant increase in the depth of internal oxidation from 206 ± 25 nm under the 223 K (-50°C) dp process atmosphere to 247 ± 35 nm under the 243 K (-30°C) process atmosphere to 1285 ± 259 nm under the 278 K ($+5^\circ\text{C}$) dp process atmosphere, respectively, for the Reference steel. Similarly, in the case of the Sn-added steel, the depth of internal oxidation increased from 51 ± 18 nm under the 223 K (-50°C) dp process atmosphere to 165 ± 36 and

627 ± 87 nm under the 243 K and 278 K (-30°C and $+5^\circ\text{C}$) dp process atmospheres, respectively.

Under the 243 K (-30°C) dp process atmosphere, the external oxide morphology was changed from large, thick, and compact plate-like and film-like particles to smaller and thinner ones after the addition of Sn, the composition of which was determined to be SiO_2 and MnSiO_3 via EELS (Figures 8(a) and (b)) in both cases. Under the 278 K ($+5^\circ\text{C}$) dp process atmosphere, internal oxides formed in two distinct morphologies in the Reference and Sn-added steels. For the Reference steel, zone I included MnSiO_3 and Mn_2SiO_4 oxide particles in both the bulk and along the grain boundaries, to a depth of approximately 500 nm. Zone II, on the other hand, defined as the area in which a network of grain boundary oxides only were observed, encompassed the region approximately $2\ \mu\text{m}$ below the surface (Figure 8(c)). Adding Sn to the steel resulted in a similar oxidation pattern and oxide composition in the steel subsurface, with the most significant difference being the overlap between zone I and zone II (Figure 8(d)). This result would indicate that Sn plays a significant role in

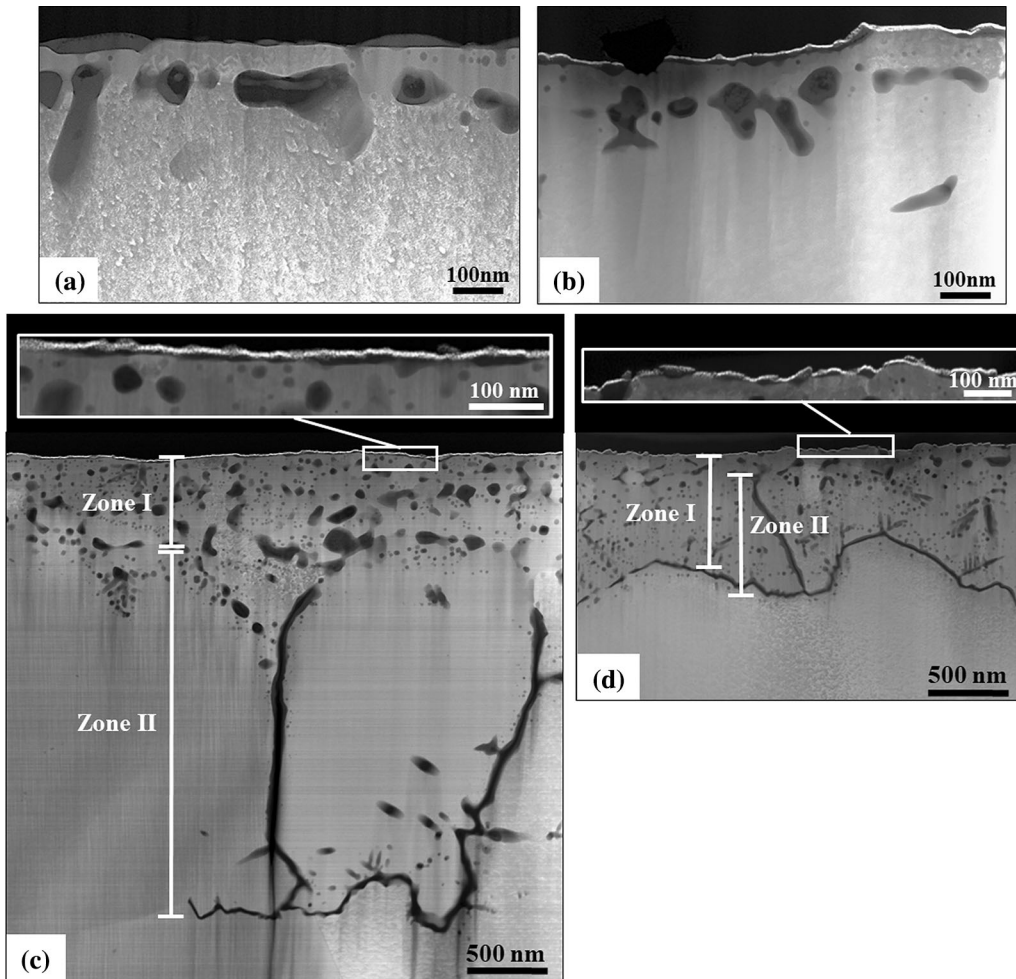


Fig. 8—TEM cross-sectional micrograph of the surface and subsurface of the (a and b) Reference and Sn-added steels, respectively, annealed under the 243 K (-30°C) dp process atmosphere and (c and d) Reference and Sn-added steels, respectively, annealed under the 278 K ($+5^\circ\text{C}$) dp process atmosphere.

slowing mass transport of O and the oxidizing species along the grain boundary network. In addition, comparing the higher magnification cross-sectional views of the external oxides of the Reference and Sn-added steels, shown in Figures 8(c) and (d), respectively, revealed that, although the oxides formed in small, compact nodule-like particles on the surface of the Reference steel (Figure 8(c)), the addition of Sn to the steel resulted in the modification of the oxide morphology to distinct, larger, and more widely spaced nodules with relatively thin inter-nodular films (Figure 8(d)), which is known to provide fewer obstacles for reactive wetting during continuous galvanizing.^[4,6] The external oxides were identified as MnSiO₃ for both the Reference and Sn-added steels *via* EELS analysis.

It is noteworthy that the significant changes observed in the oxide morphology due to the Sn addition to the steel chemistry seen in Figures 7, 8, 9 were not completely reflected in comparable changes in the Mn and Si XPS depth profiles in Figure 1, particularly for the 243 K and 278 K (−30 °C and +5 °C) dp process atmospheres. This apparent disagreement is the result of the relatively poor lateral resolution of the XPS from the 100 μm sputtering area *vs* the much high, nm-scale, resolution of TEM-EELS. Thus, the XPS spectra and results were obtained across the entire scale of the external and internal oxidation zones and were unable to resolve the fine-scale morphological changes arising from the Sn addition to the steels. Within this context, it can be seen that the two data sets are completely consistent.

Figure 9 shows a TEM micrograph and EELS elemental maps of the oxide network formed along a grain boundary of the Sn-added steel shown in Figure 8(d).

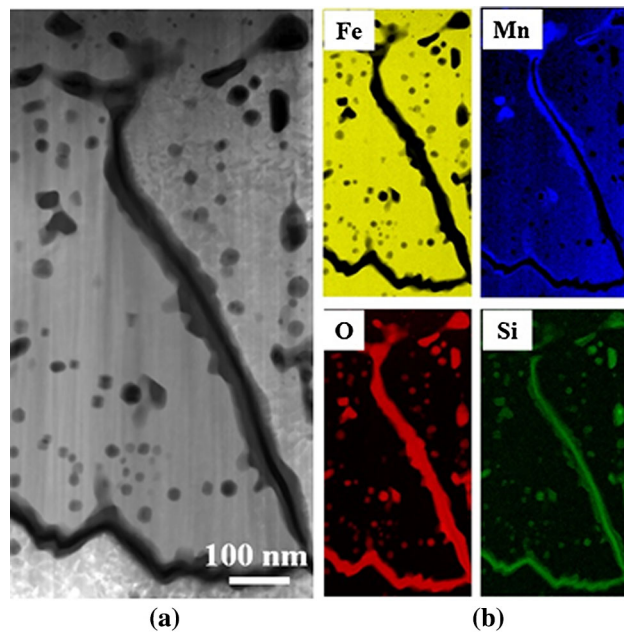


Fig. 9—(a) Detailed TEM micrograph of the oxide network formed along a grain boundary of the Sn-added steel annealed under the 278 K (+5 °C) dp process atmosphere. (b) TEM elemental maps of the oxide network.

Two different oxide compositions were expected to be identified in the oxide network as there was a difference in contrast between the core and the shell of the oxide (Figure 9(a)). The corresponding TEM elemental maps shown in Figure 9(b) indicated that, although the center of the grain boundary oxide was rich in Si, the outer shell was rich in both Si and Mn. Using EELS analysis, the outer shell and the core of the oxide network were identified as MnSiO₃ and SiO₂, respectively.

Figure 10 shows the APT results obtained to identify the elemental distribution at the steel/external oxide interface of the Sn-added steel annealed under the lowest *p*O₂ 223 K (−50 °C) dp process atmosphere for 600 seconds. Figure 10(a) provides a 3D atom map of Fe, Mn, Si, and Sn. Figure 10(b) shows a one-dimensional (1D) concentration profile generated *via* a proximity histogram (proxigram) from the 95 at. pct Fe isosurface. As can be seen, there was a Si-rich oxide transition region between the Mn-rich oxide and the Fe-rich substrate. Sn was concentrated at this interfacial region to a maximum of approximately 3 at. pct, which is roughly 150× its bulk concentration of 0.02 at. pct. It can also be seen from Figure 10(b) that there was some segregation of Sn, albeit very slight, into the external oxide, which the Mn:O ratio from the elemental profiles suggests was MnO, consistent with the previous EELS (Figure 7) and XPS (Figure 1) analyses. The existence of simultaneous Fe, Si, and O enrichment at the substrate/oxide interface beneath is likely an artifact in the APT results, due either to the known issue of O retention with analysis depth^[41] or because of the relatively rough interface from which the results are obtained.

To confirm that Sn segregation to the external surface occurred during intercritical annealing and was not present on the as-received surfaces, the as-received steel/external oxide interface was also analyzed by APT, the results of which are shown in Figure 11. Figure 11(a) shows the 3D atom map of Fe, FeO, and Ni (Ni comes from the cap deposited prior to FIB milling and is present at the base of the APT volume, with the Fe metal on the top), with elemental compositional profiles shown in Figure 11(b). As can be seen in Figure 11(b), there was a transition from the substrate to the Ni coating over a distance of approximately 6 nm. The O content increased significantly in this region, suggesting the presence of an Fe-O layer on the steel surface, as would be expected due to the exposure of the substrate to ambient O₂. This O enrichment extended slightly into the Ni layer, which is a typical artifact of APT due to preferential retention of O.^[41] Some Si enrichment can be seen just below the Fe oxide. No evidence of Sn segregation could be found at the steel/oxide interface. In order to ensure that Sn was detectable by APT and no artifact was present in the results, a concentration measurement was taken from a region of steel below the surface. The result of this analysis is shown in Table III. As can be seen, the Sn concentration was consistent with the bulk values reported in Table I. Thus, it can be concluded that there was no significant, pre-annealing Sn segregation to the oxide/substrate. This implies that any Sn enrichment arising from the hot rolling operation was removed from the interface during the pickling,

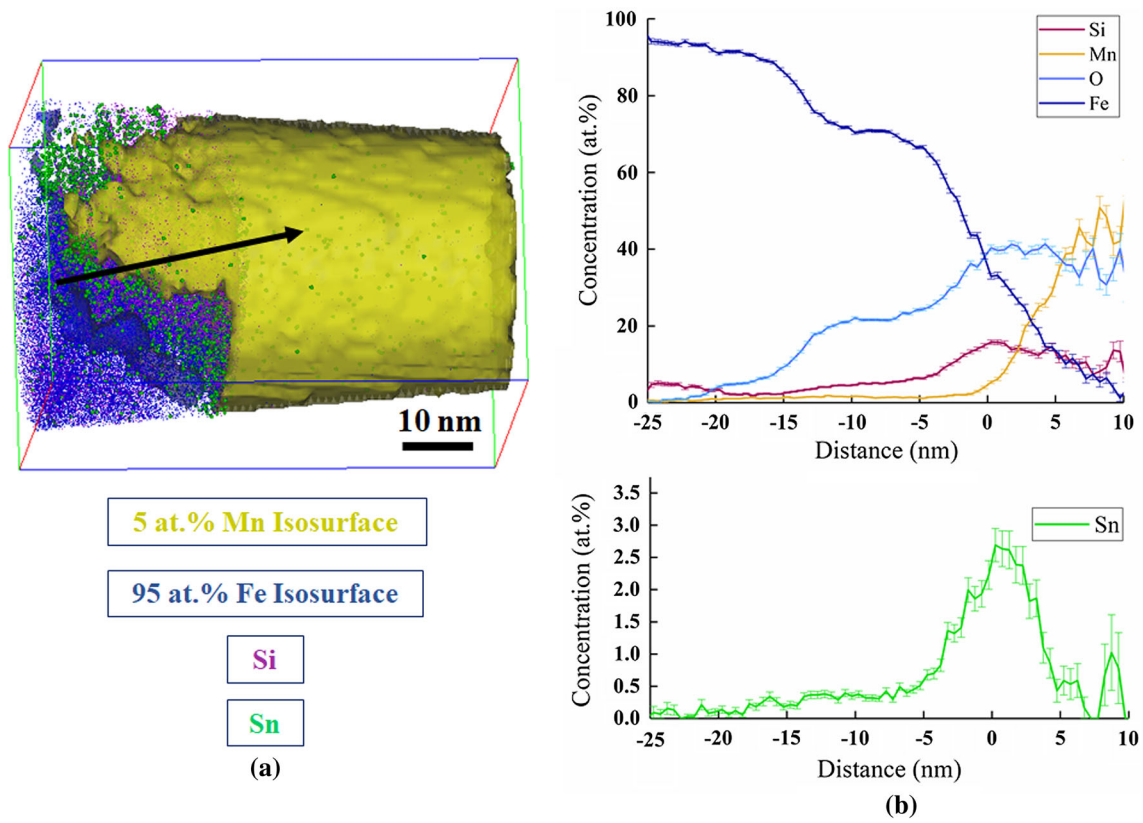


Fig. 10—(a) 3D APT atom map of the surface oxide/substrate interface of the Sn-added steel annealed under the 223 K (−50 °C) dp process atmosphere for 600 s. (b) 1D concentration profiles of Fe, O, Mn, Si, and Sn along the arrow in (a).

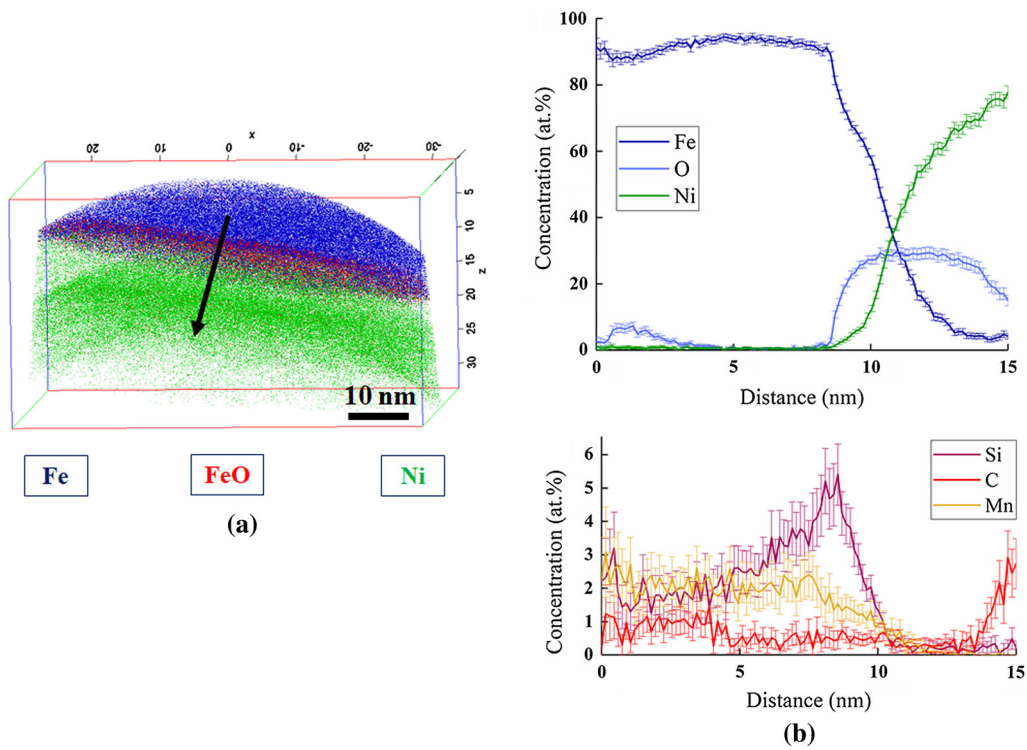


Fig. 11—(a) 3D APT atom map of the surface oxide/substrate interface of the as-received Sn-added steel. (b) 1D concentration profiles of Fe, O, Ni, Si, C, and Mn along the direction shown by the arrow in (a).

Table III. Elemental Concentration Obtained from the As-Received Sn-Added Steel Using APT

| Element | Concentration (At. Pct) | Concentration (Wt Pct) |
|---------|-------------------------|------------------------|
| Fe | 93.68 | 95.69 |
| Si | 4.168 | 2.14 |
| Mn | 2.052 | 2.06 |
| Sn | 0.0169 | 0.04 |

grinding, or sandblasting operations prior to cold rolling and annealing and that the observed Sn segregation to the external oxide/substrate interface occurred during intercritical annealing.

IV. DISCUSSION

The effects of process atmosphere oxygen partial pressure (pO_2), addition of 0.05 wt pct Sn to the steel chemistry, and annealing time on the morphology, chemistry, and growth kinetics of both external and internal oxides formed during annealing heat treatments prior to galvanizing of a Fe-0.1C-2Mn-1.7Si (wt pct) advanced high-strength steel in a simulated continuous galvanizing process were determined.

For both the Reference and Sn-added steels, as was anticipated according to the Wagner criterion,^[37] increasing the process atmosphere pO_2 *via* increasing the process atmosphere dew point was shown to encourage internal oxidation and reduce external oxidation of the alloying elements. This is exemplified by the observed decrease in the surface enrichment of Si and Mn and increase in the depth of internal oxidation per the XPS elemental depth profiles (Figure 1), as well as the lower coverage of the experimental steels' surfaces by the oxides shown in the SEM surface images (Figures 4 through 6) for the higher pO_2 process atmospheres. This finding is further supported by the greater depth at which oxides formed in the subsurface, as shown in the TEM cross-sectional micrographs (Figures 7 and 8) under the higher pO_2 243 K and 278 K (-30 °C and $+5$ °C) dp process atmospheres compared to the lowest pO_2 223 K (-50 °C) dp process atmosphere (Table II).

The occurrence of the transition from external to internal oxidation by increasing the process atmosphere pO_2 from 223 K dp to 278 K (-50 °C and $+5$ °C) dp was also confirmed by the significant decrease in the external oxide thickness and simultaneous increase in internal oxidation depth exhibited in Figures 2(a) and (b), respectively, as well as the decrease established in the growth rate constant of the external oxides shown in Figure 3(a) and consummate increase in the growth rate constant of internal oxidation in Figure 3(b), respectively. The decrease in the thickness of the film-like surface oxides obtained by increasing the atmosphere dew point from 223 K to 243 K (-50 °C to -30 °C) and the modifications which occurred in the morphology of the surface oxides from film-like to nodule-like particles by further increasing the process atmosphere pO_2 using the 278 K ($+5$ °C) dp are expected to promote reactive

wetting of the alloys during continuous galvanizing through providing conditions for the formation of the η -Fe₂Al₅Zn_x interfacial layer *via* mechanisms such as aluminothermic reduction and interfacial infiltration of the Zn(Al,Fe) continuous galvanizing bath, as has been reported by several authors.^[4,6,13,24,42]

Adding 0.05 wt pct Sn to the steel chemistry was shown to affect both the external and internal oxide morphologies and their growth kinetics. As was shown by comparing the 3D APT data from Figures 10 and 11, Sn segregation to the steel surface occurred during intercritical annealing and was not present on the as-received surface. As shown in Figure 10(b), the enrichment of Sn to the oxide/substrate interface on the Sn-added steel annealed for 600 seconds under the 223 K (-50 °C) dp process atmosphere was approximately $150\times$ times the nominal bulk concentration value, indicating a strong driving force for surface segregation. Per the oxide growth kinetics shown in Figure 2, for all process atmosphere pO_2 and annealing times, the Sn addition to the steel chemistry reduced the thickness of the external oxides and the depth of internal oxidation, in agreement with the results reported using XPS elemental depth profiles (Figure 1) and TEM cross-sectional micrographs (Figures 7 and 8). Moreover, as shown in Figure 3, the parabolic growth constants (*i.e.*, k_P values) were lowered by the addition of Sn to the substrate relative to the Reference steel annealed under the same process atmosphere. As the thickness of external oxides and depth of internal oxidation were found to have a parabolic relationship with annealing time, characteristic of solid-state diffusion-controlled oxidation, it can be concluded that the diffusion barrier function of Sn segregation reduced the inward diffusion of oxygen and outward diffusion of the alloying elements, and thus reduced the oxide growth kinetics in the alloy under a given process atmosphere pO_2 and annealing time (Figures 2 and 3).^[25,33] This hypothesis is further supported by the change in internal oxide morphology shown in Figure 8 between the Reference and Sn-added alloy, where the grain boundary oxidation depth was significantly greater for the Reference *vs* Sn-added steel.

The reduction in the compactness of granular MnO oxides under the 223 K (-50 °C) dp process atmosphere (Figures 4 and 7), as well as the alterations observed in the external oxide morphology from compact, large, and thick MnSiO₃ and SiO₂ particles to smaller, thinner, and less compact nodule-like ones under the 243 K (-30 °C) dp process atmosphere (Figures 5 and 8(a) and (b)), as well as the change in the external oxide morphology from film-like and fine, closely spaced nodule-like MnSiO₃ particles to larger, more widely spaced ones under the 278 K ($+5$ °C) dp process atmosphere (Figures 6 and 8(c) and (d)) can be attributed to the Sn effect on reducing the substrate surface energy.^[21] This result arises from Sn segregation overcoming the sum of surface energy of the oxide film and the interfacial energy of the substrate and the oxide over the substrate surface energy, as suggested by Cho *et al.*^[25] As mentioned before, the external oxide morphologies observed for the Sn-added alloy are

expected to improve reactive wetting during continuous galvanizing.

It should also be noted that, in the present case, the Reference and Sn-added external oxides were identified as MnO, SiO₂, and MnSiO₃, with no significant change in the composition of the external oxides as a result of the addition of Sn. However, it should be noted that Cho *et al.*^[25] reported a decrease in their external oxides' Mn-to-Si ratio with the addition of Sn to their low-alloy TRIP-assisted steel. This was probably due to the higher amounts of Sn added to their experimental steel compared to the current experimental steel. As mentioned previously, the amount of Sn was deliberately selected as 0.05 wt pct in this research in order to minimize or mitigate any detrimental effects on the mechanical properties of the steel.^[31,32]

It is worth mentioning that the justification for using the 600-second annealed sample for APT investigation was to provide sufficient time for Sn to attain near-equilibrium segregation to the external surface in order to increase the opportunities for detecting this segregation with the global objective of understanding the mechanism responsible for the observed changes in oxide characteristics. However, it must be mentioned that the SEM observations of the as-annealed surfaces (Figures 4 through 6) and TEM cross-sectional micrographs (Figures 7 and 8) provide ample evidence that Sn modified the oxide characteristics for the shorter annealing times of at 120 seconds. This shows that lower annealing times were ample for Sn to effectively modify the oxide morphology and spatial distribution and increase their potential applicability in the industrial process as these annealing times are more compatible with industrial practice.

Globally, the above results indicate that the use of higher dew point (higher pO_2) process atmospheres in combination with the micro-Sn addition to the steel chemistry is likely to have positive benefits with respect to the reactive wetting of this substrate by the continuous galvanizing bath. A comprehensive investigation of the reactive wetting mechanisms of the Reference and Sn-added substrates is currently underway and will be the subject of a subsequent contribution.

V. CONCLUSIONS

The combined effects of annealing time, atmosphere oxygen partial pressure, and a 0.05 wt pct Sn addition on the morphology, thickness, and chemistry of the oxides formed during annealing an experimental Fe-0.1C-2Mn-1.7Si (wt pct) AHSS under 223 K, 243 K and 278 K (−50 °C, −30 °C and +5 °C) dp process atmospheres were determined. From this investigation, it can be concluded that:

1. Increasing the annealing atmosphere pO_2 via increasing the process atmosphere dew point from 223 K to 243 K and 278 K (−50 °C to −30 °C and +5 °C) was found to encourage internal oxidation rather than external oxidation, thus decreasing the

thickness of the external oxides and increasing the depth of internal oxidation.

2. Significant Sn enrichment at the substrate/external oxide interface occurred during intercritical annealing.
3. It was determined that, in the case of the Sn-added steel, the external and internal oxidation kinetics were significantly reduced *vs* the Reference alloy, likely as a result of the observed segregation of Sn to the surface of the steel and its effect on the inward diffusion of O and the outward diffusion of the alloying elements. This reduction in kinetics manifested itself *via* a significant reduction of the parabolic rate constants for the Sn-added alloy for the growth of both the external and internal oxides.
4. The Sn addition changed the morphology of the external oxides for all annealing conditions explored. Under the 223 K (−50 °C) process atmosphere, Sn reduced the surface coverage of closely packed areas of compact granular MnO oxides. Under the 243 K (−30 °C), the addition of Sn altered the morphology of the surface oxides from film-like MnSiO₃ and SiO₂ layers comprised of large and thick particles to smaller, thinner, and less compact nodule-like oxides. Under the highest pO_2 278 K (+5 °C) dp process atmosphere, Sn modified the surface oxides from film-like and fine, closely spaced nodule-like MnSiO₃ particles to larger, more widely spaced nodules. The observed changes are very likely a consequence of the Sn segregation to the external oxide/substrate interface, locally altering the surface tension of the substrate.
5. It is expected that the changes in the external oxide morphology observed for the Sn-added alloy will have positive benefits with respect to the reactive wetting of the experimental alloy by the continuous galvanizing Zn(Al,Fe) bath, with the higher pO_2 process atmosphere, Sn-added substrate surface likely having the more optimal morphology to promote reactive wetting.

ACKNOWLEDGMENTS

The authors would like to thank Stelco Inc. and the Natural Sciences and Engineering Research Council of Canada (NSERC) for their financial support of this work through the NSERC/Stelco Industrial Research Chair in Advanced Coated Steels (Grant No. IRCPJ 305921-12). The authors also thank U.S. Steel R&D for provision of the experimental substrates. The authors are grateful to Messrs. John Thomson and Raymond Fullerton from the McMaster Steel Research Centre for assistance with the galvanizing simulations, Mr. Travis Casagrande and Dr. Andreas Korinek from the Canadian Centre for Electron Microscopy for aid with the sample analysis, and Ms. Li Sun (ArcelorMittal Dofasco) for assistance with XPS.

REFERENCES

1. P. Drillet, Z. Zermout, D. Bouleau, J. Maigne, and S. Claessens: *Rev. Métall.*, 2004, vol. 101, pp. 831–37.
2. J. Mahieu, S. Claessens, and B.C. De Cooman: *Metall. Mater. Trans. A*, 2001, vol. 32A, pp. 2905–08.
3. J. Mahieu, S. Claessens, B.C. De Cooman, and F. Goodwin: in *6th International Conference on Zinc and Zinc Alloy Coated Steel Sheet Conference*, Chicago, 2004, pp. 529–38.
4. E.M. Bellhouse: McMaster University, 2010.
5. I. Parezanović: Rheinisch-Westfälische Technische Hochschule Aachen, 2005.
6. E.M. Bellhouse and J.R. McDermid: *Metall. Mater. Trans. A*, 2010, vol. 41A, pp. 1539–53.
7. E.M. Bellhouse and J.R. McDermid: *Metall. Mater. Trans. A*, 2012, vol. 43A, pp. 2426–41.
8. M. Norden, M. Blumenau, T. Wuttke, and K.J. Peters: *Appl. Surf. Sci.*, 2013, vol. 271, pp. 19–31.
9. E.M. Bellhouse and J.R. McDermid: *Metall. Mater. Trans. A*, 2011, vol. 42A, pp. 2753–68.
10. S. Alibeigi, R. Kavitha, R.J. Meguerian, and J.R. McDermid: *Acta Mater.*, 2011, vol. 59, pp. 3537–49.
11. S. Prabhudev, S. Swaminathan, and M. Rohwerder: *Corros. Sci.*, 2011, vol. 53, pp. 2413–18.
12. R. Sagl, A. Jarosik, D. Stifter, and G. Angeli: *Corros. Sci.*, 2013, vol. 70, pp. 268–75.
13. L. Cho, S.J. Lee, M.S. Kim, Y.H. Kim, and B.C. De Cooman: *Metall. Mater. Trans. A*, 2013, vol. 44A, pp. 362–71.
14. H. Liu, Y. He, S. Swaminathan, M. Rohwerder, and L. Li: *Surf. Coat. Technol.*, 2011, vol. 206, pp. 1237–43.
15. V.F.C. Lins, L. Madeira, J.M.C. Vilela, M.S. Andrade, V.T.L. Buono, J.P. Guimarães, and E.A. Alvarenga: *Appl. Surf. Sci.*, 2011, vol. 257, pp. 5871–78.
16. M.S. Kim, J.H. Kwak, J.S. Kim, Y.H. Liu, N. Gao, and N.Y. Tang: *Metall. Mater. Trans. A*, 2009, vol. 40A, pp. 1903–10.
17. K. Kahoul and M. Turchetto: in *10th International Conference on Zinc Zinc Alloy Coated Steel Sheet Conference*, Toronto, 2015, pp. 436–43.
18. Y.F. Gong and B.C. De Cooman: *Iron Steel Inst. Jpn. Int.*, 2011, vol. 51, pp. 630–37.
19. M. Seah: *Acta Metall.*, 1980, vol. 28, pp. 955–62.
20. M.P. Seah: *J. Catal.*, 1979, vol. 57, pp. 450–57.
21. M.P. Seah and E.D. Hondros: *Proc. R. Soc. Lond. A.*, 1973, vol. 335, pp. 191–212.
22. H. Viehhaus and M. Rusenberg: *Surf. Sci.*, 1985, vol. 159, pp. 1–23.
23. L. Yin and S. Sridhar: *Metall. Mater. Trans. B*, 2010, vol. 41B, pp. 1095–1107.
24. L. Cho, M.S. Kim, Y.H. Kim, and B.C. De Cooman: *Metall. Mater. Trans. A*, 2014, vol. 45A, pp. 4484–98.
25. L. Cho, E.J. Seo, G.S. Jung, D.W. Suh, and B.C. De Cooman: *Metall. Mater. Trans. A*, 2016, vol. 47A, pp. 1705–19.
26. G. Lyudkovsky: *IEEE Trans. Magn.*, 1986, vol. 22, pp. 508–10.
27. E. Clauberg, C. Uebing, and H.J. Grabke: *Appl. Surf. Sci.*, 1999, vol. 143, pp. 206–14.
28. Z.T. Zhang, I.R. Sohn, F.S. Pettit, G.H. Meier, and S. Sridhar: *Metall. Mater. Trans. B*, 2009, vol. 40B, pp. 550–66.
29. Z.T. Zhang, I.R. Sohn, F.S. Pettit, G.H. Meier, and S. Sridhar: *Metall. Mater. Trans. B*, 2009, vol. 40B, pp. 567–84.
30. D.S. Petrovic, M. Jenko, V. Gontarev, and H.J. Grabke: *Kovine Zlitine Tehmol.*, 1998, vol. 32, pp. 493–96.
31. D.A. Melford: *Proc. R. Soc. Lond. A.*, 1980, vol. 295, pp. 89–103.
32. Y. Li, J.P. Han, Z.H. Jiang, and P. He: *Int. J. Miner. Metall. Mater.*, 2015, vol. 22, pp. 37–44.
33. M. Pourmajidian, B. Langelier, and J.R. McDermid: *Metall. Mater. Trans. A*, 2018, vol. 49A, pp. 5561–73.
34. K. Thompson, D. Lawrence, D.J. Larson, J.D. Olson, T.F. Kelly, and B. Gorman: *Ultramicroscopy*, 2007, vol. 107, pp. 131–39.
35. C.R. Brundle, C.A. Evans, and S. Wilson, Jr.: *Encyclopedia of Materials Characterization*, Butterworth-Heinemann, Boston, 1992.
36. N. Birks, G.H. Meier, and F.S. Pettit: *Introduction to the High-Temperature Oxidation of Metals*, Cambridge University Press, Cambridge, 2006.
37. C. Wagner: *Zh. Elektrochem.*, 1959, vol. 63, pp. 772–82.
38. A.P. Grosvenor, E.M. Bellhouse, A. Korinek, M. Bugnet, and J.R. McDermid: *Appl. Surf. Sci.*, 2016, vol. 379, pp. 242–48.
39. H.K. Schmid and W. Mader: *Micron*, 2006, vol. 37, pp. 426–32.
40. C.C. Ahn and O.L. Krivanek: with contributions by: R.P. Burgner, M.M. Disko, and P.R. Swann, *EELS Atlas. A Reference Guide of Electron Energy Loss Spectra Covering All Stable Elements*, Gatan Inc., Warrendale, 1983.
41. E.A. Marquis, B.P. Geiser, T.J. Prosa, and D.J. Larson: *J. Microscopy*, 2011, vol. 241, pp. 225–33.
42. G. Seyed Mousavi and J.R. McDermid: *Surf. Coat. Technol.*, 2018, vol. 351, pp. 11–20.

Publisher's Note Springer Nature remains neutral with regard to jurisdictional claims in published maps and institutional affiliations.